IJCRT.ORG ISSN : 2320-2882

INTERNATIONAL JOURNAL OF CREATIVE RESEARCH THOUGHTS (IJCRT)

An International Open Access, Peer-reviewed, Refereed Journal

Investigation Of Magnetic Induction And Slip Effects In Peristaltic Flow Of A Micropolar Fluid: An Analytical Approach

A. Sinha
Department of Mathematics, Yogoda Satsanga Palpara Mahavidyalaya, Palpara, Purba Medinipur, west Bengal, India-721458

ABSTRACT

This study investigates the peristaltic transport of a micropolar fluid in an asymmetric channel under the influence of an induced magnetic field. The effects of slip velocity at the channel boundaries are incorporated into the analysis. By employing the long wavelength and low Reynolds number approximations, analytical expressions for the axial velocity, stream function, magnetic force function, and axial induced magnetic field are derived. The governing expressions are evaluated for a specific set of parameter values used in the model analysis. The computed results are illustrated graphically to highlight the physical behavior of the flow. It is observed that variations in the parameters significantly influence the flow characteristics, and the presence of a magnetic field notably affects the fluid motion. The influence of slip velocity on the flow exhibits a behavior similar to that of the induced magnetic field.

Keywords: Peristalsis; Micropolar Fluid; Slip velocity; Induced Magnetic Field; Pressure Gradient

1 Introduction

Peristaltic motion, a mechanism of fluid transport driven by progressive wave propagation along a boundary, has become an important subject of study due to its wide physiological and engineering significance. It plays a key role in processes such as urine, chyme, sperm, and ovum transport, and in blood flow through small vessels. Industrially, this mechanism is used for transporting slurries and corrosive fluids and in the functioning of peristaltic pumps like roller and finger pumps.

The pioneering analysis of peristaltic motion was undertaken by Latham [1], marking the beginning of systematic research in this area. Since then, numerous contributions, both theoretical and experimental [2–9], have enhanced our understanding of peristaltic mechanisms in different physical and physiological situations. However, most existing studies have modeled blood and other physiological fluids as Newtonian, an assumption appropriate for peristaltic transport in the ureter but inadequate for describing complex biological flows such as those in small blood vessels, lymphatic vessels, the intestine, and reproductive tracts. The models proposed by Shapiro et al. [10] and Shapiro [11] were highly idealized, representing peristaltic motion as an infinite train of sinusoidal waves propagating through a two-dimensional channel. Their analyses primarily aimed to explain the important phenomenon of reflux, in which fluid is transported in the direction opposite to the mean flow. A notable example of such reflux occurs when bacteria migrate from the bladder to the kidneys against the normal urinary flow. Subsequently, Srivastava and Srivastava [12] investigated the peristaltic motion of an incompressible Newtonian viscous fluid containing a suspension of small, spherical, rigid particles in a channel with flexible walls.

Research on peristaltic motion in electrically conducting physiological fluids has gained significant attention owing to its biomedical and engineering applications. These studies provide valuable insights into the working principles of devices such as blood pumps and MRI systems, and aid in enhancing the performance of MHD peristaltic compressors. Li et al. [13] reported that impulsive magnetic fields can serve as an effective therapeutic tool for patients with urinary stone fragments. Hakeem et al. [14] investigated the influence of an applied magnetic field on peristaltic motion within a uniform tube containing a fluid of variable viscosity. Misra et al. [15] conducted a theoretical study on the peristaltic transport of physiological fluid in a porous asymmetric channel under the effect of a magnetic field. Wang et al. [16] examined the peristaltic motion of a magneto-micropolar fluid in a symmetric tube, employing the assumptions of long wavelength and low Reynolds number. However, in all these investigations, the effect of the induced magnetic field was neglected, even though such an effect may not be insignificant, particularly when the magnetic Reynolds number is small. Considering the limitations of earlier models that ignored magnetic induction, Shit et al. [17] analyzed the peristaltic flow of a micropolar fluid in an asymmetric uniform channel under the influence of an induced magnetic field. Their findings indicated that the inclusion of magnetic induction significantly influences the flow field, pressure rise per wavelength, and streamline pattern. Mekheimer [18,19] extended this line of research by studying induced magnetic field effects in symmetric channels for both couple stress and micropolar fluids.

Though the no-slip condition is central to classical fluid mechanics, it fails in some cases where a partial velocity slip occurs between the fluid and the wall. This behavior is observed in particulate fluids or rarefied gases with finite Knudsen numbers, where intermolecular interactions at the boundary are insufficient to enforce the no-slip constraint. Beavers and Joseph [20] formulated a modified boundary condition that expresses the slip velocity at a permeable or coated boundary in terms of the tangential velocity and shear stress. This condition has wide-ranging significance in both biological and engineering contexts, especially where the interaction between the fluid and the boundary is weak or modified by surface treatments. Examples include the polishing and lubrication of artificial heart valves, flow through micro- and nanochannels, and applications involving thin lubricating films or hydrophobic coatings like octadecyltrichlorosilane [21]. Recognizing its practical importance, a number of investigators [22–25] have extended the study of slip effects to peristaltic motion of physiological fluids. These investigations demonstrate that wall slip can modify the flow resistance, streamline pattern, and trapping phenomena, thereby providing a more realistic description of flow behavior in biological and technological systems.

A thorough review of the available literature reveals that no prior investigation has been reported on the peristaltic transport of a micropolar fluid in an asymmetric channel considering the combined effects of wall slip and induced magnetic field. The no-slip boundary condition, though widely applied in continuum fluid mechanics, proves inadequate in cases where the fluid exhibits macroscopic slip at the wall. Such situations demand a modified boundary formulation that relates the slip velocity to the wall traction through an appropriate physical law.

Keeping this aspect in view, the present work is aimed at developing a theoretical model for the magnetohydrodynamic peristaltic motion of a micropolar fluid, incorporating the effects of both induced magnetic field and velocity slip. The study seeks to bridge the gap between idealized theoretical assumptions and realistic flow conditions encountered in biological systems and microfluidic devices, thereby enriching the understanding of MHD peristaltic phenomena.

2 Modelling

We analyze the peristaltic motion of an incompressible viscous fluid flowing through an asymmetric two-dimensional channel in the presence of an externally applied magnetic field. Since the fluid is electrically conducting, its motion gives rise to an induced magnetic field, and both effects are included in the formulation to describe the magnetohydrodynamic peristaltic transport more accurately. Let us assume that $Y' = h_1'$ and $Y' = h_2'$ be respectively the upper wall and lower wall of the channel (cf. Figure 1). The medium is considered to be induced by a sinusoidal wave train propagating with a constant speed c along the channel wall, such that

$$h_1'(X',t') = d_1 + a_1 \cos\left[\frac{2\pi}{\lambda}(X' - ct')\right] \quad on\,the\,upper\,boundary, \tag{1}$$

$$h_2'(X',t') = -d_2 - a_2 \cos\left[\frac{2\pi}{\lambda}(X'-ct')+\phi\right] \quad on\,the\,lower\,boundary, \tag{2}$$

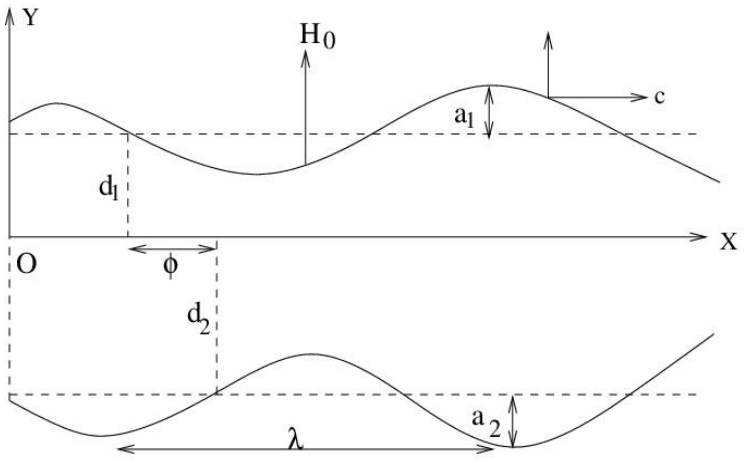

Figure 1: A Physical sketch of the problem

where a_1 and a_2 are the amplitudes of waves, λ is the wave length, $\phi(0 \le \phi \le \pi)$ the phase difference, X' and Y' are the rectangular co-ordinates with X' measures the axis of the channel and Y' the traverse axis perpendicular to X'.

A constant magnetic field of strength H_0 is applied in the transverse direction. This gives rise to an induced magnetic field $H'(h_x', h_y', 0)$ and therefore the total magnetic field will be $H'^{+}(h_x', H_0 + h_y', 0)$, where h_x' and h_y' are the components of induced magnetic field along the co-ordinate axes.

In the present analysis, the flow of an incompressible magneto-micropolar fluid is considered under the assumption that body couples are negligible. Accordingly, the governing equations representing the conservation of mass, momentum, microrotation, and magnetic field are expressed as:

$$\vec{\nabla}' \cdot \vec{v}' = 0 \tag{3}$$

$$\rho\left(\frac{\partial \vec{v}'}{\partial t'} + (\vec{v}' \cdot \vec{\nabla}')\vec{v}'\right) = -\vec{\nabla}'\left(p' + \frac{1}{2}\mu_e (H'^{+})^2\right) + (\mu + k)\nabla'^2 \vec{v}' + k\vec{\nabla}' \times \vec{w}' - \mu_e\left(\vec{H}'^{+} \cdot \vec{\nabla}'\right)\vec{H}'^{+} \tag{4}$$

$$\rho j\left(\frac{\partial \vec{w}'}{\partial t'} + (\vec{v}' \cdot \vec{\nabla}')\vec{w}'\right) = -2k\vec{w}' + k\vec{\nabla}' \times \vec{v}' - \gamma\left(\vec{\nabla}' \times \vec{\nabla}' \times \vec{w}'\right) + (\alpha + \beta + \gamma)\vec{\nabla}'(\vec{\nabla}' \cdot \vec{w}') \tag{5}$$

The Maxwell's equations,

$$\vec{\nabla}' \times \vec{H}'^{+} = \vec{J}', \qquad \vec{\nabla}' \times \vec{E}' = -\mu_e\left(\frac{\partial \vec{H}'^{+}}{\partial t'}\right) \tag{6}$$

along with the Ohm's law

$$\vec{J}' = \sigma\left(\vec{E}' + \mu_e(\vec{v}' \times \vec{H}'^{+})\right) \tag{7}$$

in addition, it should be noted that

$$\vec{\nabla}' \cdot \vec{H}' = 0 \;\; and \;\; \vec{\nabla}' \cdot \vec{E}' = 0 \tag{8}$$

Now, combining equations (6) - (8) we get the induction equation,

$$\frac{\partial \vec{H}'^{+}}{\partial t'} = \vec{\nabla}' \times (\vec{v}' \times \vec{H}'^{+}) + \frac{1}{\mu_e \sigma}\nabla'^2 \vec{H}'^{+} \tag{9}$$

where $\frac{1}{\mu_e \sigma}(=\eta)$ is the magnetic diffusivity, $\nabla'^2 \equiv \frac{\partial^2}{\partial X'^2} + \frac{\partial^2}{\partial Y'^2}$ and v' is the velocity vector, ω' is the microrotation vector, p' is the fluid pressure, ρ the fluid density, j the micro-gyration parameter, σ the electrical conductivity, μ_e is the magnetic permeability, E' is an induced electrical field. Also the

material constants (or viscosity coefficients of the micro-polar fluid) μ and k are satisfies the following inequalities $(2\mu+k)\geq 0$, $k\geq 0$.

The governing equations $(3)-(5)$ and the magnetic induction equation (9) will be solved subject to the boundary conditions defined in the next section.

3 Solution

It is further noticed that the flow field in laboratory frame (X',Y') and wave frame $(x'.y')$ are treated as the unsteady and steady motion respectively. Considering the wave frame (x',y') moving with a velocity c away from a fixed frame (X',Y') that follows from the following transformations

$x'=X'-ct', \quad y'=Y', \quad u'(x',y')=U'-c, \quad v'(x',y')=V'.$

In which (u',v') and (U',V') are the respective velocity components in the laboratory and wave frames.

The fundamental equations governing the unsteady flow of an incompressible magneto-micropolar fluid are derived in a Cartesian coordinate system, taking into account the coupling between the fluid velocity, microrotation, and magnetic field, and are expressed as follows.

$$\frac{\partial U'}{\partial X'}+\frac{\partial V'}{\partial Y'}=0 \tag{10}$$

$$\frac{\partial U'}{\partial t'}+U'\frac{\partial U'}{\partial X'}+V'\frac{\partial U'}{\partial Y'}=-\frac{1}{\rho}\frac{\partial p'}{\partial X'}+\frac{\mu+k}{\rho}\left(\frac{\partial^2 U'}{\partial X'^2}+\frac{\partial^2 U'}{\partial Y'^2}\right)+\frac{k}{\rho}\frac{\partial w'}{\partial Y'}-\frac{\mu_e}{\rho}\left(h_x'\frac{\partial h_x'}{\partial X'}+h_y'\frac{\partial h_x'}{\partial Y'}\right)-\frac{\mu_e}{\rho}H_0\frac{\partial h_x'}{\partial Y'} \tag{11}$$

$$\frac{\partial V'}{\partial t'}+U'\frac{\partial V'}{\partial X'}+V'\frac{\partial V'}{\partial Y'}=-\frac{1}{\rho}\frac{\partial p'}{\partial X'}+\frac{\mu+k}{\rho}\left(\frac{\partial^2 V'}{\partial X'^2}+\frac{\partial^2 V'}{\partial Y'^2}\right)+\frac{k}{\rho}\frac{\partial w'}{\partial X'}$$
$$-\frac{\mu_e}{\rho}\left(h_x'\frac{\partial h_y'}{\partial X'}+h_y'\frac{\partial h_y'}{\partial Y'}\right)-\frac{\mu_e}{\rho}H_0\frac{\partial h_y'}{\partial Y'} \tag{12}$$

$$\rho j\left(\frac{\partial w'}{\partial t'}+U'\frac{\partial w'}{\partial X'}+V'\frac{\partial w'}{\partial Y'}\right)=-2kw'+k\left(\frac{\partial V'}{\partial X'}-\frac{\partial U'}{\partial Y'}\right)+\gamma\left(\frac{\partial^2 w'}{\partial X'^2}+\frac{\partial^2 w'}{\partial Y'^2}\right) \tag{13}$$

Let us introduce the following non-dimensional variables

$$x=\frac{x'}{\lambda}, y=\frac{y'}{a}, u=\frac{u'}{c}, v=\frac{\lambda v'}{ac}, \omega=\frac{a\omega'}{c}, h(x)=\frac{h'(x')}{a}, p=\frac{a^2 p'(x')}{\lambda\mu c}$$
$$t=\frac{ct'}{\lambda}, J=\frac{j}{a^2}, \psi=\frac{\psi'}{ca}, \zeta=\frac{\zeta'}{H_0 a}, h_x=\frac{h_x'}{H_0} \quad and \quad h_y=\frac{h_y'}{H_0} \tag{14}$$

where ψ and ζ represent the dimensionless stream function and magnetic force function respectively.

On introducing the dimensionless variables defined in equation (11)-(13) into the preceding equations, the governing equations can be rewritten in the following dimensionless form.

$$R_e\delta\left[\left(\psi_y\frac{\partial}{\partial x}-\psi_x\frac{\partial}{\partial y}\right)\psi_y\right]=-\frac{\partial P_m}{\partial x}+\frac{1}{1-N}\nabla^2\psi_y+\frac{N}{1-N}\frac{\partial\omega}{\partial y}+R_e S^2\zeta_{yy}$$
$$+R_e S^2\delta\left[\left(\zeta_y\frac{\partial}{\partial x}-\zeta_x\frac{\partial}{\partial y}\right)\zeta_y\right] \tag{15}$$

$$R_e\delta^3\left[\left(\psi_x\frac{\partial}{\partial y}-\psi_y\frac{\partial}{\partial x}\right)\psi_x\right]=-\frac{\partial P_m}{\partial y}-\frac{\delta^2}{1-N}\nabla^2\psi_x-\frac{\delta^2 N}{1-N}\frac{\partial\omega}{\partial x}-R_e S^2\delta^2\zeta_{xy}$$
$$-R_e S^2\delta^3\left[\left(\zeta_y\frac{\partial}{\partial x}-\zeta_x\frac{\partial}{\partial y}\right)\zeta_x\right] \tag{16}$$

$$R_e\delta J\frac{1-N}{N}\left[\left(\psi_y\frac{\partial}{\partial x}-\psi_x\frac{\partial}{\partial y}\right)\omega\right]=-2\omega-\nabla^2\psi+\frac{2-N}{m^2}\nabla^2\omega \quad (17)$$

$$\psi_y-\delta(\psi_x\zeta_y-\psi_y\zeta_x)+\frac{1}{R_m}\nabla^2\zeta=E \quad (18)$$

with

$$u=\frac{\partial\psi}{\partial y}, v=-\frac{\partial\psi}{\partial x}, h_x=\frac{\partial\zeta}{\partial y}, h_y=-\delta\frac{\partial\zeta}{\partial x}, \nabla^2\equiv\delta^2\frac{\partial^2}{\partial x^2}+\frac{\partial^2}{\partial y^2}. \quad (19)$$

The following dimensionless parameters that appear in (15) - (19) are defined as

$R_e=\frac{ca\rho}{\mu}$ the Reynolds number , $\delta=\frac{a}{\lambda}$ the Wave number, $S=\frac{H_0}{c}\sqrt{(\frac{\mu_e}{\rho})}$ the Strommer's number is also known as magnetic force number, $R_m=\sigma\mu_e ac$ the magnetic Reynolds number, $N=\frac{k}{k+\mu}$, $(0\le N\le 1)$ the coupling parameter and $m^2=\frac{a^2k(2\mu+k)}{(\gamma(\mu+k))}$ is the micropolar or microrotation parameter.

The total pressure in the fluid, which is equal to the sum of the ordinary and magnetic pressure given by $P_m=p+\frac{1}{2}R_e\delta(\frac{\delta(H^+)^2}{\rho c^2})$, and $E(=-\frac{E'}{\mu_e cH_0})$ is defined as the electrical field strength in non-dimensional form.

Eliminating the total pressure from equations (15) and (16), the resulting equation can be written as

$$R_e\delta\left[\left(\psi_y\frac{\partial}{\partial x}-\psi_x\frac{\partial}{\partial y}\right)\nabla^2\psi\right]=\frac{1}{1-N}\nabla^4\psi+\frac{N}{1-N}\nabla^2\omega$$
$$+R_eS^2\nabla^2\zeta_y+R_eS^2\delta\left[\left(\zeta_y\frac{\partial}{\partial x}-\zeta_x\frac{\partial}{\partial y}\right)\nabla^2\zeta\right] \quad (20)$$

The instantaneous volumetric flow rate in the fixed frame is given by

$$Q=\int_{h_2'}^{h_1'}U'(X',Y',t')dy' \quad (21)$$

where h_1' and h_2' are functions of X' and t'.

The rate of volume flow in the wave frame is found to be given by

$$q=\int_{h_2'}^{h_1'}u'(x',y')dy' \quad (22)$$

where h_1', and h_2' are function of X' alone.

We note that $h_1(x)$ and $h_2(x)$ represent the dimensionless form of the peristaltic channel walls given by the equations of the form

$$h_1(x)=1+a\cos(2\pi x), \quad h_2(x)=-d-b\cos(2\pi x+\phi) \quad (23)$$

where, $a=\frac{a_1}{d_1}$, $b=\frac{a_2}{d_1}$, $d=\frac{d_2}{d_1}$.

Using the transformation into the equations (21) and (22), the relation between Q and q can be obtained as

$$Q=q+c(h_1'-h_2') \quad (24)$$

The time mean flow over a period T at a fixed position X' is defined as

$$Q'=\frac{1}{T}\int_0^T Qdt \quad (25)$$

Using (24) in (25) the flow rate Q' has the form

$$Q'=\frac{1}{T}\int_0^T qdt+c(h_1'-h_2')=q+cd_1+cd_2 \quad (26)$$

The non-dimensional form of equation (26) is given by

$$\theta=F+1+d \quad (27)$$

where $\theta = \frac{Q'}{cd_1}$ and $F = \frac{q}{cd_1}$,

such that

$$F = \int_{h_2}^{h_1} \frac{\partial \psi}{\partial y} dy = \psi(h_1) - \psi(h_2) \tag{28}$$

The boundary conditions for the dimensionless stream function $\psi(x, y)$ and magnetic force function $\zeta(x, y)$ in the wave frame can be put mathematically as,

$$\frac{\partial \psi}{\partial y} + \beta \frac{\partial^2 \psi}{\partial y^2} = -1 \, on \, y = h_1$$

$$\frac{\partial \psi}{\partial y} + \beta \frac{\partial^2 \psi}{\partial y^2} = -1 \, on \, y = h_2$$

$$\omega = 0 \, on \, y = h_1 \, and \, y = h_2$$

$$\psi = \frac{F}{2} \, on \, y = h_1$$

$$= -\frac{F}{2} \, on \, y = h_2$$

$$and \, \zeta = \frac{\partial \zeta}{\partial y} = 0 \, on \, y = h_1 \, and \, y = h_2 \tag{29}$$

where β is consider as the slip parameter. Applying long wave length approximation $(\delta = 1)$ and assuming the Reynolds number to be small, the dimensionless equations (20), (17) and (18) becomes

$$\frac{\partial^4 \psi}{\partial y^4} + N \frac{\partial^2 \omega}{\partial y^2} + R_e S^2 (1 - N) \frac{\partial^3 \zeta}{\partial y^3} = 0 \tag{30}$$

$$\frac{(2 - N)}{m^2} \frac{\partial^2 \omega}{\partial y^2} = 2\omega + \frac{\partial^2 \psi}{\partial y^2} \tag{31}$$

$$\frac{\partial^2 \zeta}{\partial y^2} = R_m (E - \frac{\partial \psi}{\partial y}) \tag{32}$$

By operating $\frac{\partial^2}{\partial y^2}$ and $\frac{\partial}{\partial y}$ on both sides of (31) and (32) respectively and substituting the expressions for $\frac{\partial^4 \psi}{\partial y^4}$ and $\frac{\partial^3 \zeta}{\partial y^3}$ in the equation (30) we obtain

$$\frac{\partial^4 \omega}{\partial y^4} - \{m^2 + (1 - N) H^2\} \frac{\partial^2 \omega}{\partial y^2} + \frac{2m^2 H^2 (1 - N)}{(2 - N)} \omega = 0 \tag{33}$$

Again, substituting the expression of $\frac{\partial^2 \omega}{\partial y^2}$ from (31) and $\frac{\partial^3 \zeta}{\partial y^3}$ from (32) after differentiating with respect to y, in the expression (30) the stream function ψ may be written as

$$\psi = \frac{1}{H^2 (1 - N)} \left[\frac{(2 - N)}{m^2} \{ \frac{\partial^2 \omega}{\partial y^2} - m^2 \omega \} + C_1 y + C_2 \right] \tag{34}$$

where $H^2 = R_e S^2 R_m$ i.e, $H = (\mu_e H_0) a \sqrt{\frac{\sigma}{\mu}}$ is the Hartmann number and C_1 and C_2 are two integrating constants which are to be determined.

The general solution of equation (33) takes in the form,

$$\omega = A \cosh(\theta_1 y) + B \sinh(\theta_1 y) + C \cosh(\theta_2 y) + D \sinh(\theta_2 y), \tag{35}$$

where

$$\theta_1 = \frac{1}{\sqrt{2}}\sqrt{\{(1-N)H^2+m^2\}+\sqrt{\{(1-N)H^2+m^2\}^2-\frac{8m^2(1-N)H^2}{(2-N)}}}$$

and $$\theta_2 = \frac{1}{\sqrt{2}}\sqrt{\{(1-N)H^2+m^2\}-\sqrt{\{(1-N)H^2+m^2\}^2-\frac{8m^2(1-N)H^2}{(2-N)}}}$$

together with four integrating constants A, B, C and D.

Using the corresponding boundary conditions for ω in equations (34) and (35), the stream function ψ has the form

$$\psi = \frac{1}{H^2(1-N)}[\frac{(2-N)}{m^2}\{(\theta_1^2-m^2)(A\cosh(\theta_1 y)+B\sinh(\theta_1 y))$$
$$+(\theta_2^2-m^2)(C\cosh(\theta_2 y)+D\sinh(\theta_2 y))\}+C_1 y+C_2] \quad (36)$$

Applying the boundary conditions given in the equation (29) into the expressions ω and ψ the values of all the constants have been determined and are given in the appendix.

Thus, the expressions for the axial velocity u and stream function ψ are obtained as

$$u = \frac{\partial\psi}{\partial y} = \frac{1}{Z_0}\left[Z_1\{A\sinh(\theta_1 y)+B\cosh(\theta_1 y)\}+Z_2\{C\sinh(\theta_2 y)+D\cosh(\theta_2 y)\}+C_1\right] \quad (37)$$

and $$\psi(x,y) = \frac{1}{Z_0}\left[\frac{Z_1}{\theta_1}\{A\cosh(\theta_1 y)+B\sinh(\theta_1 y)\}+\frac{Z_2}{\theta_2}\{C\cosh(\theta_2 y)+D\sinh(\theta_2 y)\}+C_1 y+C_2\right] \quad (38)$$

Now solving the equation (32) with the corresponding equation (38) , we get the magnetic force function ζ as

$$\zeta(x,y) = R_m E\frac{y^2}{2}-\frac{R_m}{Z_0}\left[\frac{Z_1}{\theta_1^2}\{A\sinh(\theta_1 y)+B\cosh(\theta_1 y)\}\right.$$
$$\left.+\frac{Z_2}{\theta_2^2}\{C\sinh(\theta_2 y)+D\cosh(\theta_2 y)\}+C_1\frac{y^2}{2}+C_2\right]+C_3 y+C_4 \quad (39)$$

where the constants C_3 and C_4 are obtained so far using the boundary conditions (29) are also included in the appendix.

The corresponding mathematical expressions for the axial-induced magnetic field and the distribution of current density across the channel can be written, respectively, as follows. $h_x = \frac{\partial\zeta}{\partial y} = R_m E y - R_m\psi + C_3$ (40)

and

$$J_z = R_m E - R_m u. \quad (41)$$

The electric field strength E can be determined by integrating (32) and using the boundary conditions on ζ and ψ across the wall surface as

$$E = \frac{F}{h_1(x)-h_2(x)} \quad (42)$$

Using equation (15), the relationship describing the pumping characteristics of the peristaltic flow in terms of the axial pressure gradient is derived and may be written as follows.

$$\frac{\partial p}{\partial x} = \frac{1}{(1-N)}\frac{\partial^3\psi}{\partial y^3}+\frac{N}{(1-N)}\frac{\partial\omega}{\partial y}+H^2(E-\frac{\partial\psi}{\partial y}). \quad (43)$$

With the help of equations (35) and (38), the axial pressure gradient governing the flow field is derived and written in the following form.

$$\frac{\partial p}{\partial x} = \frac{1}{z_0(1-N)}\{Z_1\theta_1^2(A\sinh(\theta_1 y)+B\cosh(\theta_1 y))+Z_2\theta_2^2(C\sinh(\theta_2 y)+D\cosh(\theta_2 y))\}$$
$$+\frac{N}{(1-N)}\{A\theta_1(sinh(\theta_1 y)+B\theta_1\cosh(\theta_1 y)+C\theta_2\sinh(\theta_2 y)+D\theta_2\cosh(\theta_2 y)\}$$
$$+H^2(E-u) \quad (44)$$

The pressure rise per wave length Δp in the non-dimensional form is given by

$$\Delta p = \int_0^1 \frac{\partial p}{\partial x} dx \tag{45}$$

One of the characteristic features of micropolar fluids is that their stress tensor is non-symmetric, unlike in classical viscous fluid theory. This asymmetry arises due to the micro-rotational effects of fluid particles. Therefore, in the present analysis, the dimensionless shear stress components are represented by the following expressions.

$$\tau_{xy} = \frac{\partial u}{\partial y} - \frac{N}{(1-N)}\omega \tag{46}$$

$$\tau_{yx} = \frac{1}{(1-N)}\frac{\partial u}{\partial y} + \frac{N}{(1-N)}\omega \tag{47}$$

The numerical computations for the shear stresses τ_{xy} and τ_{yx} are obtained at both the upper and lower walls of the channel and whose graphical representation is presented in the next section.

4 Computational Results

Analytical expressions for the flow and magnetic field variables—namely the axial velocity, pressure rise, axial induced magnetic field, current density, wall shear stress, stream function, and magnetic force function—have been derived in the previous section. To gain physical insight into the behavior of the flow, numerical computations based on these expressions have been carried out. The input parameters used for the computation have been adopted from the existing studies reported in the literature [7, 17, 25]: $a = b = 0.5$, $d = 1.0$, $m = 0.1$, $R_m = 0.01$, $\theta = 2.4$, $H = 0.001, 2, 4, 8, 16$, $N = 0.2, 0.4, 0.6, 0.8$, $\phi = 0, \frac{\pi}{2}, \frac{3\pi}{4}, \pi$ and $\beta = 0.0, 0.5, 1.0, 1.5$.

Figures 2-4 illustrate the variation of axial velocity for different values of the Hartmann number (H), slip parameter (β), and micropolar coupling parameter (N). From Figure 2, it is evident that the axial velocity decreases near the centerline of the channel as the Hartmann number H increases. This behavior occurs because a stronger magnetic field produces a greater Lorentz force, which acts as a retarding force on the fluid motion. As a result, the velocity of the fluid in the central region is suppressed. However, near the channel walls, a slight acceleration in the fluid velocity is observed, which helps maintain a constant volumetric flow rate for all values of H. This indicates that while the magnetic field redistributes the velocity profile, it does not alter the overall flow rate through the channel. In Figure 3, the effect of the slip parameter β on the axial velocity is presented. It is observed that as the slip parameter increases, the velocity at the wall becomes higher, whereas the velocity near the center of the channel decreases. Physically, this is because the partial slip condition allows the fluid to move more freely along the wall, reducing frictional resistance. Consequently, a portion of the momentum that would normally be dissipated at the boundary is instead retained within the fluid, leading to an enhancement of near-wall velocity and a corresponding decrease in core velocity.

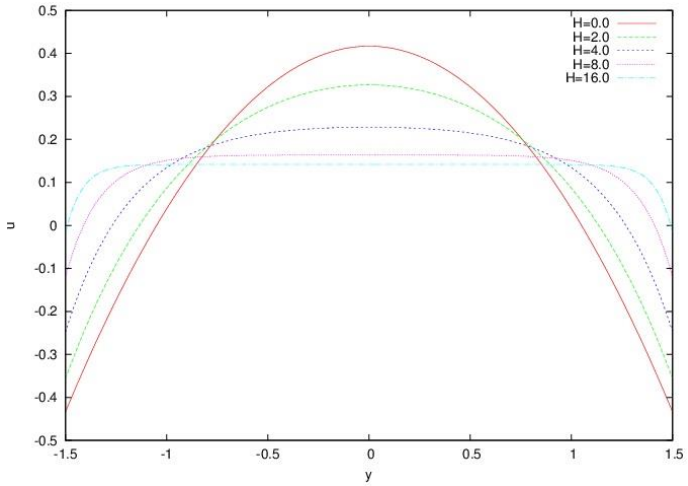

Figure 2: Variation of axial velocity u for different values of H with $N = 0.4, \phi = 0.0, \beta = 0.5$

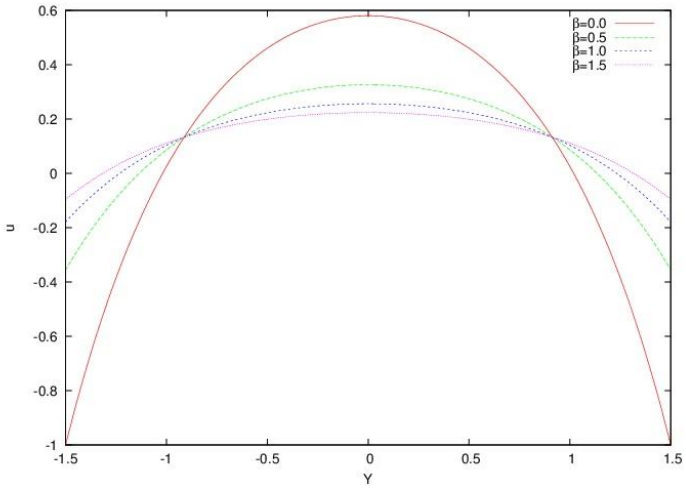

Figure 3: Variation of axial velocity u for different values of β with $H = 2.0, N = 0.4, \phi = 0.0$

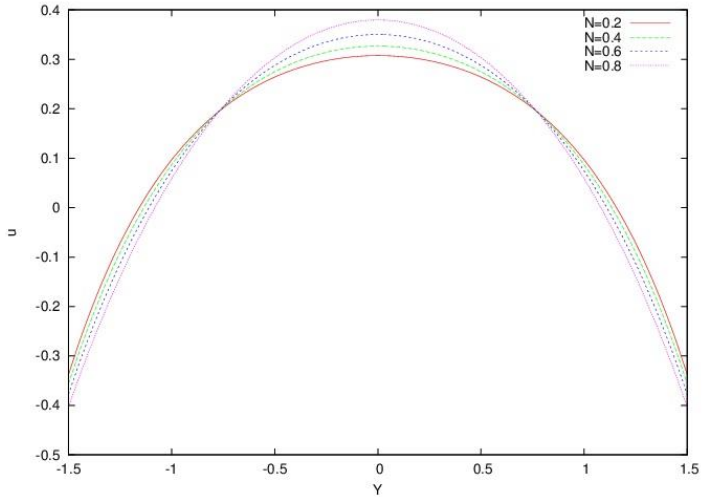

Figure 4: Variation of axial velocity u for different values of N with $H = 2.0, \phi = 0.0, \beta = 0.5$

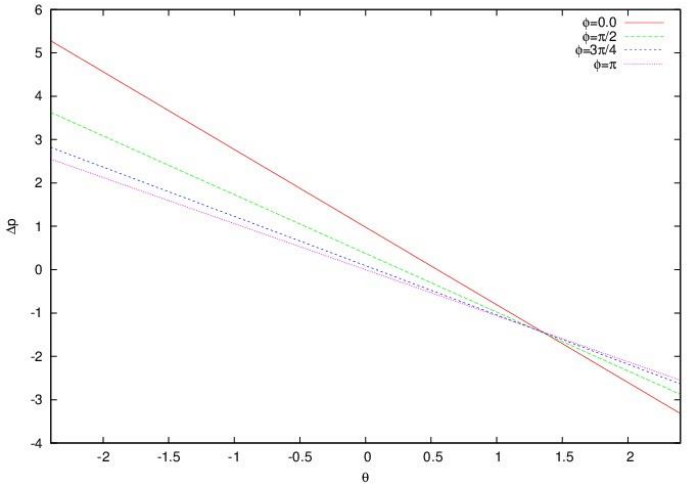

Figure 5: Variation of pressure rise ΔP with θ for different values of ϕ with $N = 0.4, H = 2.0, \beta = 0.5$

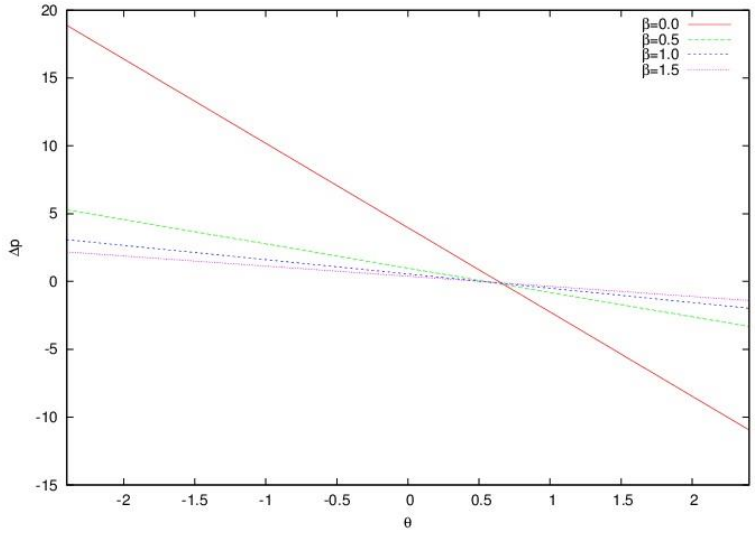

Figure 6 Variation of pressure rise ΔP with θ for different values of β with $H = 2.0, N = 0.4, \phi = 0.0,$

However, the trend is reversed in the case of the micropolar coupling parameter (N), as illustrated in Figure 4. The presence of micro-rotational particles significantly influences the flow behavior by introducing additional rotational motion, which enhances the effective viscosity of the fluid and alters the velocity distribution across the channel. As the coupling parameter increases, the interaction between the microelements and the base fluid becomes stronger, leading to noticeable modifications in the flow field.

The variation of pressure rise (Δp) with respect to the dimensionless volumetric flow rate (Q) is presented in Figures 5 and 6. It is observed that the pressure rise varies linearly with the flow rate, indicating a direct proportionality between these two quantities. Specifically, the pressure rise decreases linearly as the volumetric flow rate increases, which is a typical characteristic of peristaltic motion under low Reynolds number conditions. The pumping phenomenon can be categorized into three distinct regions based on the sign and magnitude of the pressure rise (Δp):The region where Δp>0 corresponds to pumping, further classified as positive pumping when Q>0 and negative pumping when Q<0; The region for which Δp<0 is known as co-pumping; The case Δp=0 represents the free pumping condition. From Figure 6, it is evident that the pressure rise (Δp) decreases with increasing phase difference (φ) in both the pumping and free-pumping regions, while a transition occurs in the co-pumping region. A similar behavior is observed in Figure 3 for different values of the slip parameter (β). However, an interesting feature emerges from the figure — in the absence of slip (i.e., when β=0), the magnitude of the pressure rise is considerably higher. This indicates that the introduction of slip velocity reduces the resistance to flow, thereby decreasing the required pressure to maintain the same volumetric flow rate.

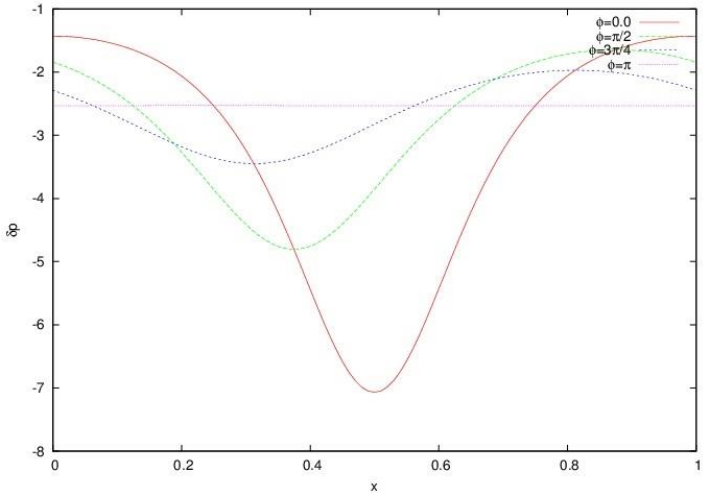

Figure 7: Distribution of pressure gradient $\delta P = \frac{\partial p}{\partial x}$ for different values of ϕ with $H = 2.0, N = 0.4, \beta = 0.5$

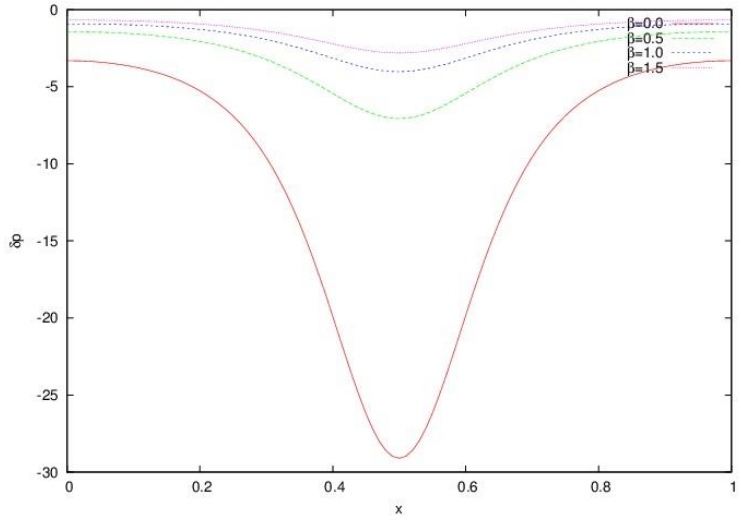

Figure 8: Distribution of pressure gradient $\delta P = \frac{\partial p}{\partial x}$ for different values of β with $H = 2.0, N = 0.4, \phi = 0.0,$

Figure 7 and Figure 8 show the variation of axial pressure gradient $\frac{\partial p}{\partial x}$ along the length of the channel in one wave length. Figure 7 indicates that the peak value of the magnitude of the axial pressure gradient decreases with increasing phase difference ϕ. One can note from this figure that when the phase difference is 180^0, no change in the pressure gradient is observed. The peak value of the pressure gradient shifted onwards along the phase difference ϕ. Figure 8 depicts the variation of axial pressure gradient with various slip parameters β. It is shown that the magnitude of the pressure gradient gradually decreases with the increase of the slip parameters β.

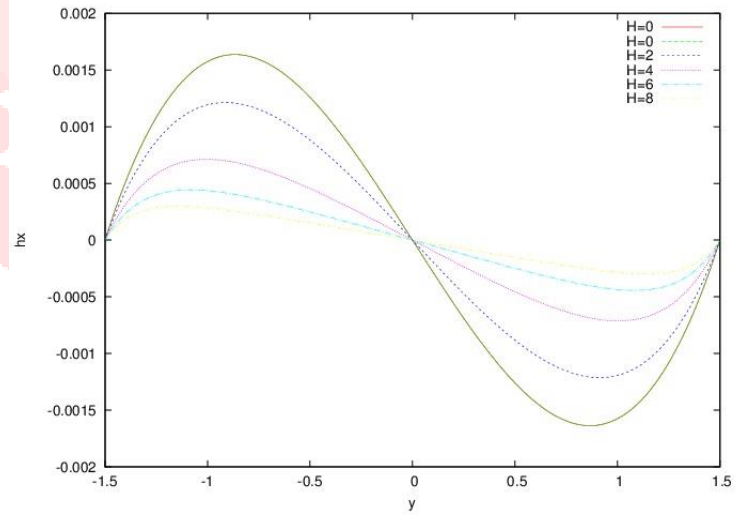

Fig. 9 Effect of axial induced magnetic field h_x for different values of H with $N = 0.4, \phi = 0.0, \beta = 0.5$

Figures 9 and 10 illustrate the influence of the induced magnetic field on the flow characteristics for varying values of the Hartmann number (H) and the slip parameter (β). As shown in Figure 9, the magnitude of the axial induced magnetic field (h_x) decreases with increasing Hartmann number. This behavior arises because a stronger applied magnetic field enhances the Lorentz force, which suppresses the fluid motion and, consequently, the generation of the induced magnetic component. In other words, as the imposed magnetic field becomes dominant, the fluid-induced magnetic response diminishes. From Figure 10, it is evident that the induced magnetic field is also significantly affected by the slip parameter. An increase in the slip parameter leads to a further reduction in the magnitude of the induced field. This is because the wall slip condition decreases the frictional interaction between the fluid and the channel boundaries, thereby weakening the current generation mechanism responsible for inducing magnetic

effects in the flow domain. It is also observed from these figures that the induced magnetic field (h_x) is positive near the lower wall, where the external magnetic field is applied, and negative near the upper wall. This behavior indicates that the induced field circulates in opposite directions about the channel's centerline, forming two distinct magnetic lobes. These lobes represent regions of opposing magnetic polarity resulting from the recirculating nature of the induced currents in the conducting fluid. As the slip parameter increases, the centers of these lobes are observed to shift toward the channel walls, implying that the induced magnetic activity becomes confined closer to the boundaries as wall slip effects intensify

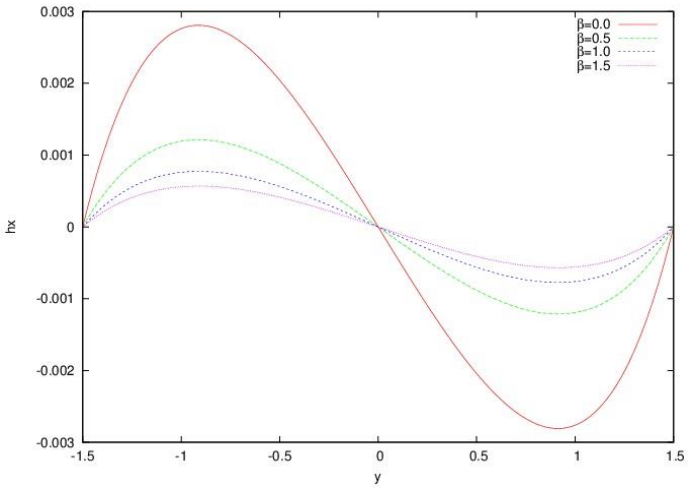

Figure 10: Effect of axial induced magnetic field h_x for different values of β with $H = 2.0, N = 0.4, \phi = 0.0,$

The distribution of current density J_z for the variation of Hartmann number H and the slip parameter β are illustrated in Figure 11 and Figure 12. Figure 11 shows that the current density becomes flattening and decreases at the central region with increasing the magnetic field strength. Similarly, from Figure 12, we observed that the current density also decreases at the central region of the channel, whereas it is enhances near the wall with the increasing values of the slip parameter β.

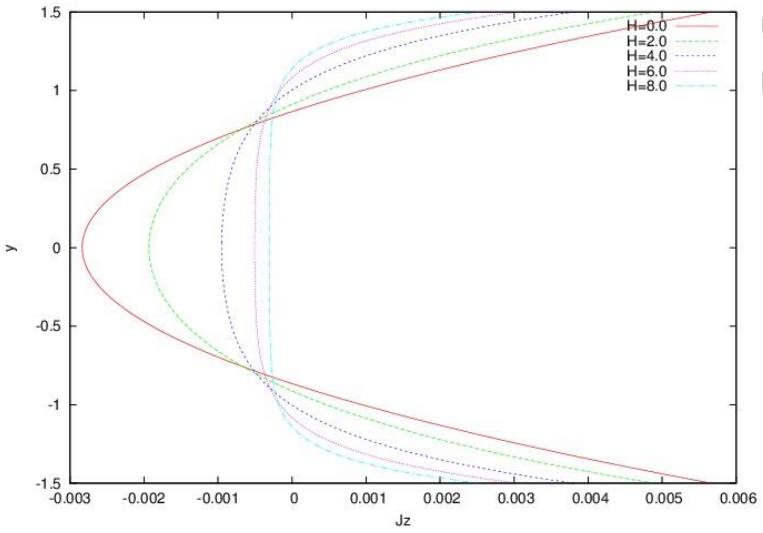

Figure 11: Distribution of current density J_z for different values of H with $N = 0.4, \phi = 0.0, \beta = 0.5$

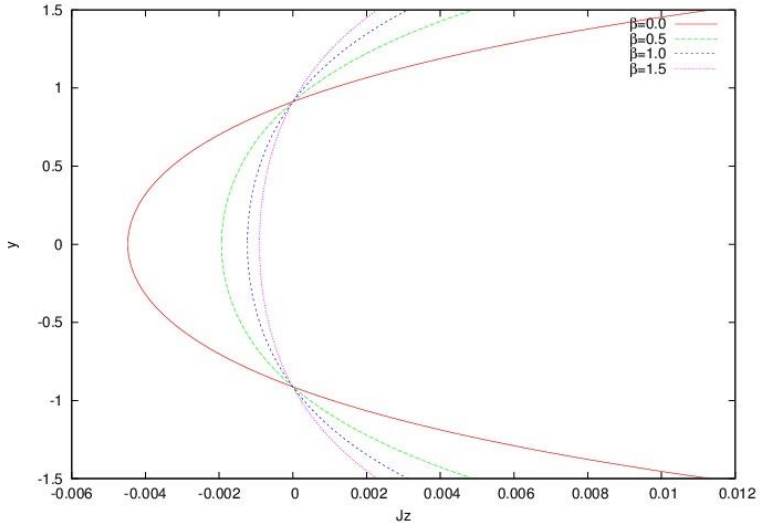

Figure 12: Distribution of current density J_z for different values of β with $H = 2.0, N = 0.4, \phi = 0.0,$

Figures 13−15 exhibit the distribution of wall shear stress τ_{xy} with the variation of slip parameters β, phase difference ϕ between the walls of the channel and the micropolar coupling parameter N. We observe from Figure 13 that the magnitude of the wall shear stress decreases with an increase in the slip parameter β. The magnitude of the wall shear stress is always greater in the case of no-slip velocity condition at the wall. It is interesting to seen from Figure 14 that the magnitude of the shear stress on both the walls decreases with the increase of the phase difference ϕ. However the peak value of the wall shear stress shifted backward direction as the wave train moves on the forward direction. Therefore, the asymmetric channel has a significant impact on the wall shear stress. The non-Newtonian effect for the micropolar fluid due to the coupling parameter N has also significant role in controlling the distribution of wall shear stress as shown in Figure 15. We observe that as the coupling parameter N increases, the magnitude of the wall shear stress decreases.

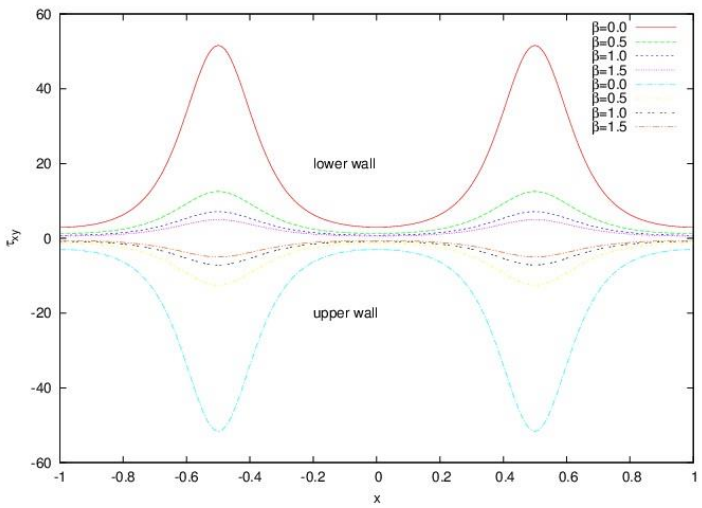

Fig. 13 Variation of τ_{xy} along with the co-ordinate x for different values of β with $H = 2.0$, $N = 0.4$, $\phi = 0.0$

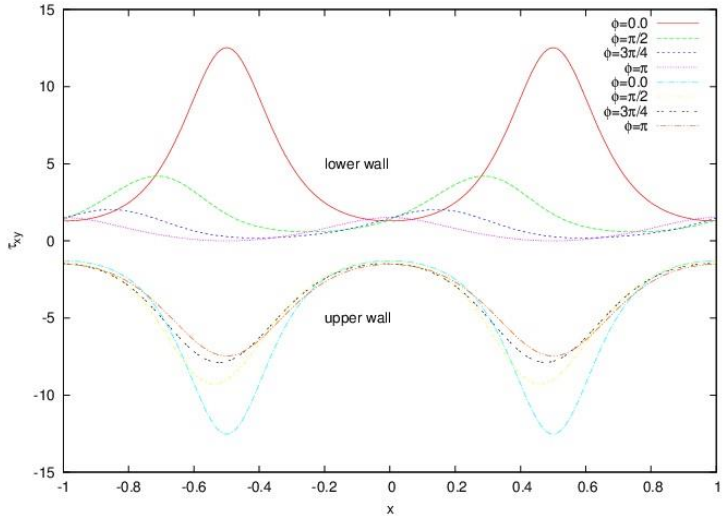

Figure 14: Variation of τ_{xy} along with the co-ordinate x for different values of ϕ with $H = 2.0$, $N = 0.4$, $\beta = 0.5$

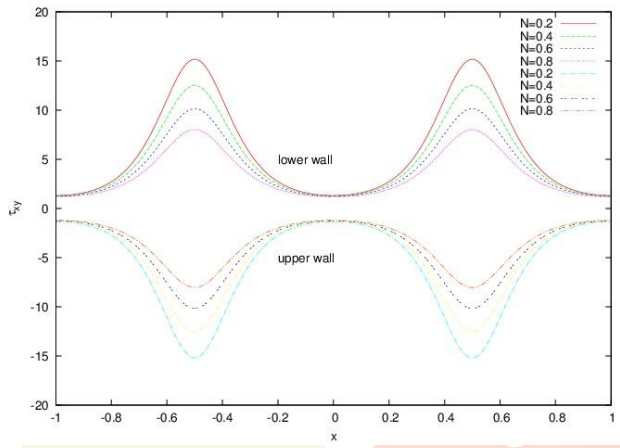

Figure 15: Variation of τ_{xy} along with the co-ordinate x for different values of N with $H = 2.0, \beta = 0.5$, $\phi = 0.0$

It is known that the phenomenon of trapping is the formation of an interesting circulating bolus of the fluid is a region of closed streamlines that move with the speed in the wave frame. Owing to the trapping phenomenon, there will exist stagnation points, where both the velocity components of the fluid vanish in the wave frame. To see the effect of various non-dimensional parameters on the streamlines are depicted in Figures $16-23$. We observe from Figures $16-18$ that the formation of trapped bolus decreases in size and vanishes with the increase of the slip parameter β. In the presence of strong slip velocity the trapped bolus eliminated and the streamlines become parallel to the channel walls. Similarly from Figures 19,17,20 and 21 we have seen that trapped bolus decreases significantly as the magnetic field strength increases. It is interesting to note from Figure 17 that when $\phi = 0$, the bolus appears and moves towards left with decreases in size as the phase difference ϕ increases as shown in Figure 22. However, when $\phi = \pi$, the trapped bolus completely disappear and streamlines aligned parallel to one another as presented in Figure 23.

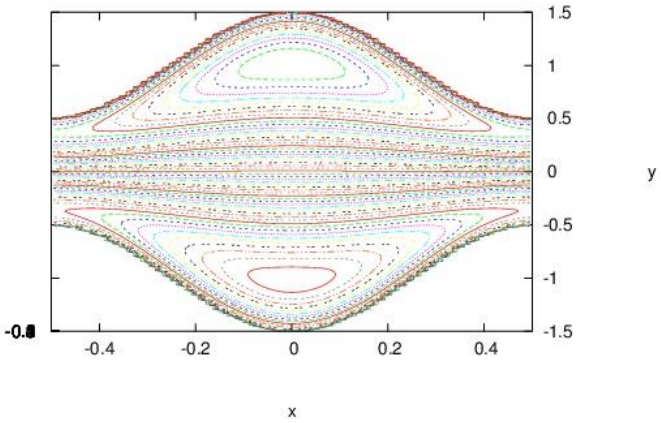

Figure 16: Streamlines pattern (ψ_{max} = 0.40945,ψ_{min} = –0.40945) for $\beta = 0.0$ with $\phi = 0.0$, $H = 2.0$, $N = 0.4$

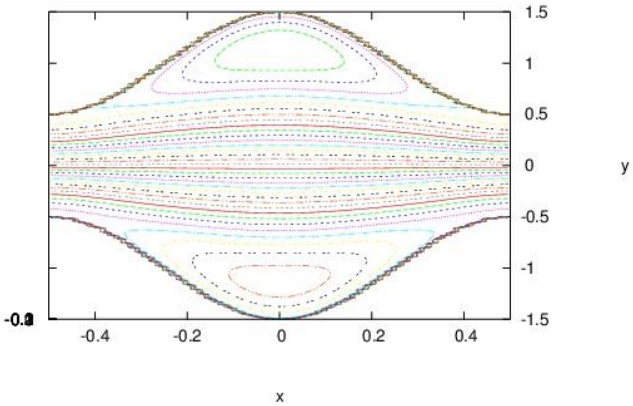

Figure 17: Streamlines pattern (ψ_{max} = 0.2587,ψ_{min} = –0.2687) for $\beta = 0.5$ with $\phi = 0.0$, $H = 2.0$, $N = 0.4$

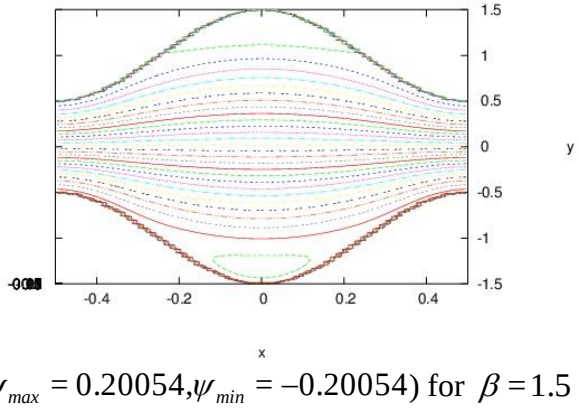

Figure 18: Streamlines pattern (ψ_{max} = 0.20054,ψ_{min} = –0.20054) for $\beta = 1.5$ with $\phi = 0.0$, $H = 2.0$, $N = 0.4$

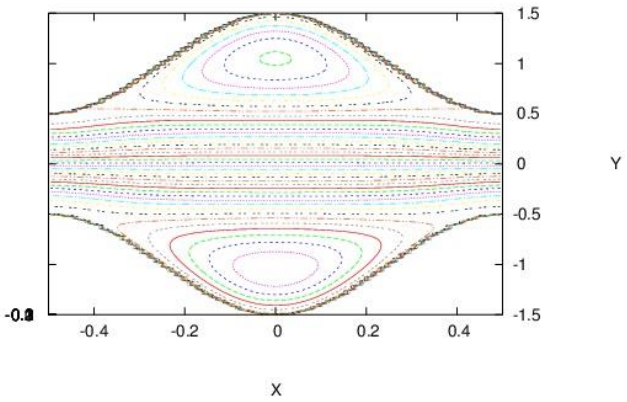

Figure 19: Streamlines pattern ($\psi_{max} = 0.29177, \psi_{min} = -0.29177$) for $H = 0$ with $\phi = 0.0$, $N = 0.4$, $\beta = 0.5$

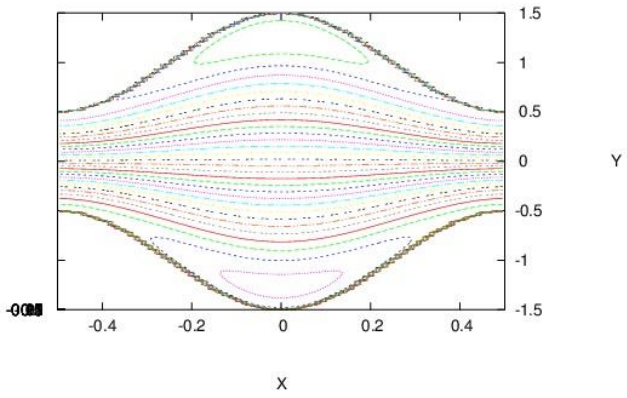

Figure 20: Streamlines pattern ($\psi_{max} = 0.22518, \psi_{min} = -0.22518$) for $H = 4$ with $\phi = 0.0$, $N = 0.4$, $\beta = 0.5$

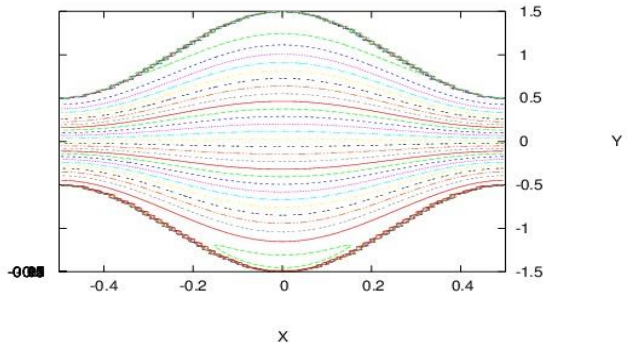

Figure 21: Streamlines pattern ($\psi_{max} = 0.20742, \psi_{min} = -0.20742$) for $H = 6$ with $\phi = 0.0$, $N = 0.4$, $\beta = 0.5$

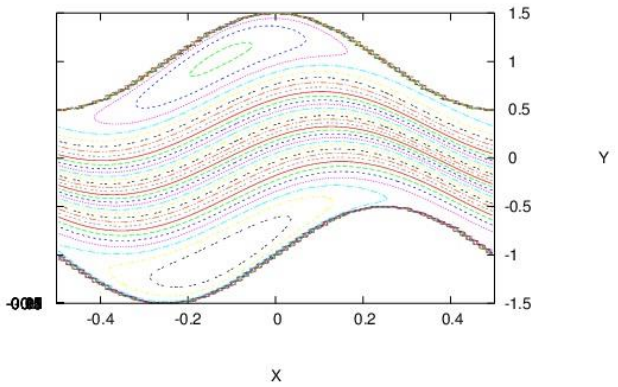

Figure 22: Streamlines pattern (ψ_{max} = 0.23978,ψ_{min} = –0.23978) for $\phi = \pi/2$ with $H = 2.0$, $N = 0.4$, $\beta = 0.5$

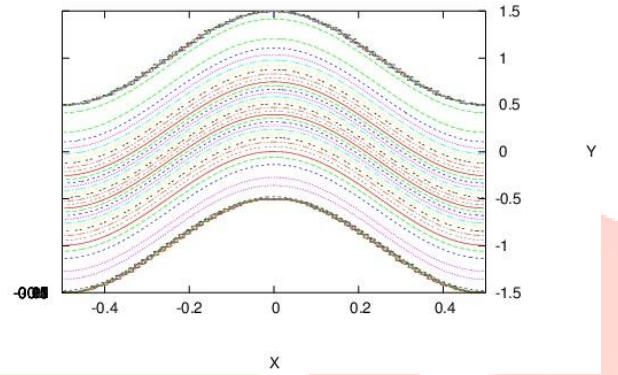

Figure 23: Streamlines pattern (ψ_{max} = 0.22099,ψ_{min} = –0.22101) for $\phi = \pi$ with $H = 2.0$, $N = 0.4$, $\beta = 0.5$

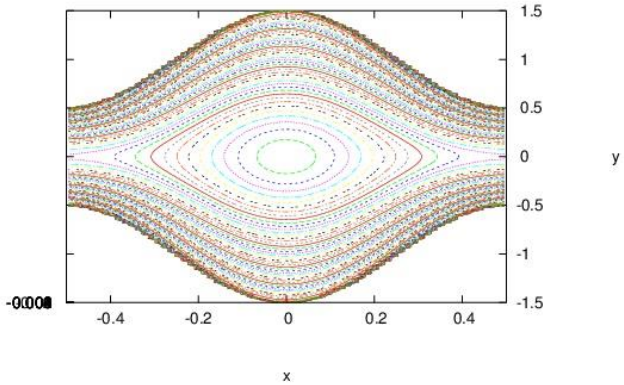

Figure 24: Distribution of magnetic force function $\zeta(x, y)$ for $\beta = 0.0$ with $N = 0.4$, $\phi = 0.0, H = 2.0$

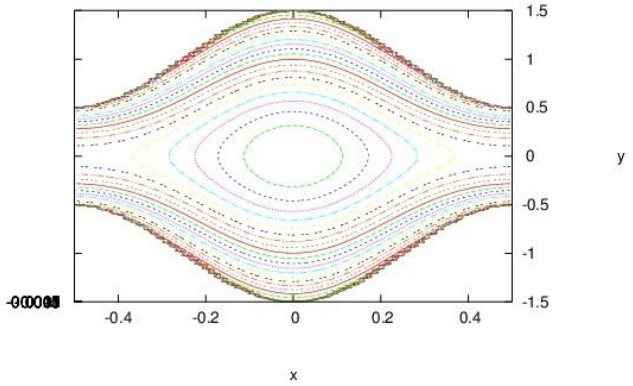

Figure 25: Distribution of magnetic force function $\zeta(x, y)$ for $\beta = 0.5$ with $N = 0.4,\ \phi = 0.0,\ H = 2.0$

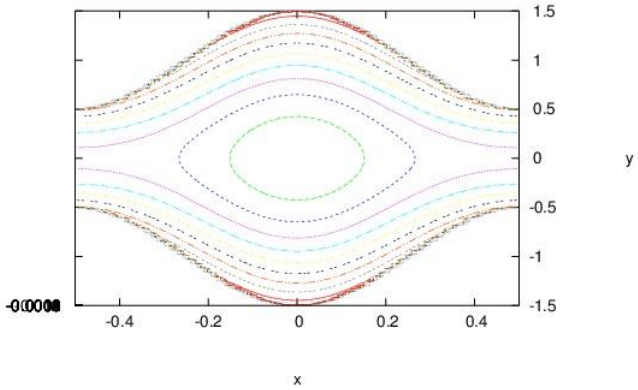

Figure 26: Distribution of magnetic force function $\zeta(x, y)$ for $\beta = 1.5$ with $N = 0.4,\ \phi = 0.0,\ H = 2.0$

The variation of the magnetic force function for different values of the slip parameter (β) is illustrated in Figures 24-26. It is observed from these figures that the number of magnetic force lines decreases as the slip parameter increases. This indicates a reduction in the magnetic field intensity within the flow region due to the enhanced wall slip, which weakens the interaction between the fluid motion and the magnetic field. The study of Shit et al. [17] reported that, in the presence of a low magnetic field strength, the magnetic lines of force are concentrated predominantly in the central region of the channel. However, these lines tend to disperse and diminish as the Hartmann number (H) increases, reflecting the suppression of induced magnetic effects by a stronger applied field. A similar trend is observed in the present analysis for the case of increasing slip velocity. Therefore, both the magnetic field strength and the wall slip parameter exhibit analogous influences on the magnetic field distribution. The introduction of slip at the channel boundaries reduces the shear interaction between the fluid and the wall, leading to a weaker induced magnetic response and consequently fewer magnetic force lines across the channel. This demonstrates that the slip mechanism and magnetic field effects act in a complementary manner, both tending to diminish the overall magnetic influence in the flow domain.

5 Conclusions:

The combined effects of slip velocity and induced magnetic field on the peristaltic transport of a micropolar fluid in an asymmetric channel have been analyzed under the long wavelength and low Reynolds number approximations. The present investigation has focused on examining how the slip condition at the wall and the induced magnetic field influence the transport characteristics of a physiological fluid. The major findings of this study can be summarized as follows:

- The axial velocity in the central region of the channel decreases with an increase in both the Hartmann number (H) and the velocity slip parameter (β).
- The viscosity parameter exhibits an enhancing effect on the axial velocity near the channel center.
- The asymmetry of the channel, introduced through the phase difference between the upper and lower walls, leads to a reduction in the magnitude of the axial pressure gradient.
- The slip velocity and induced magnetic field produce similar influences on the streamline patterns, both tending to alter the flow structure in comparable ways.

In conclusion, the present theoretical analysis provides valuable insights into the mechanisms governing magnetohydrodynamic peristaltic motion in micropolar fluids. These findings may serve as a useful reference for biomedical engineering applications, particularly in the design and optimization of magnetically controlled peristaltic pumps, blood flow modeling, and microfluidic transport systems.

Acknowledgements: This study was supported by the Seed Money Grant for Research & Development provided by Y. S. Palpara Mahavidyalaya, Palpara, Purba Medinipur, India. The author expresses sincere gratitude to Prof. (Dr.) Pradipta Kumar Mishra, Principal of the college, for his guidance and for making available the necessary research facilities.

Appendix

The expressions that appear in section 3 are listed as follows:

$$A=\frac{-[B\sinh(\theta_1 h_2)+C\cosh(\theta_2 h_2)+D\sinh(\theta_2 h_2)]}{\cosh(\theta_1 h_2)},$$

$$B=\frac{Z_{28}-CZ_{30}-DZ_{31}}{Z_{29}},\ C=\frac{Z_{39}-DZ_{41}}{Z_{40}},\ D=\frac{Z_{40}Z_{36}-Z_{37}Z_{39}}{Z_{40}Z_{38}-Z_{37}Z_{41}},$$

$$C_1=-[Z_0+Z_3A+Z_4B+Z_5C+Z_6D],$$

$$C_2=Z_0\frac{F}{2}-\frac{Z_1}{\theta_1}[A\cosh(\theta_1 h_1)+B\sinh(\theta_1 h_1)]-\frac{Z_2}{\theta_2}[C\cosh(\theta_2 h_1)+D\sinh(\theta_2 h_1)]-C_1 h_1,$$

$$C_3=\frac{1}{(h_2-h1)}[RmE\left(\frac{h_1^2-h_2^2}{2}\right)-\frac{Rm}{Z_0}[\frac{Z_1}{\theta_1^2}(A(\sinh(\theta_1 h_1)-\sinh(\theta_2 h_2))+B(\cosh(\theta_1 h_1)-\cosh(\theta_2 h_2)))$$

$$+\frac{Z_2}{\theta_2^2}(C(\sinh(\theta_2 h_1)-\sinh(\theta_2 h_2))+D(\cosh(\theta_2 h_1)-\cosh(\theta_2 h_2)))]+C_1\frac{(h_1^2-h_2^2)}{2}],$$

$$C_4=-RmE\frac{h_1^2}{2}+\frac{Rm}{Z_0}[\frac{Z_1}{\theta_1^2}(A\sinh(\theta_1 h_1)+B\cosh(\theta_1 h_1))+\frac{Z_2}{\theta_2^2}(C\sinh(\theta_2 h_1)+D\cosh(\theta_2 h_1))$$

$$+C_1\frac{h_1^2}{2}+C_2]-C_3 h_1,$$

$$\xi_1=\theta_1^2-m^2\ ,$$

$$\xi_2=\theta_2^2-m^2,\ Z_0=H^2(1-N),\quad Z_1=\frac{(2-N)\xi_1\theta_1}{m^2},\quad Z_2=\frac{(2-N)\xi_2\theta_2}{m^2},$$

$$Z_3=Z_1\sinh(\theta_1 h_1)+\beta Z_1\theta_1\cosh(\theta_1 h_1),\ Z_4=Z_1\cosh(\theta_1 h_1)+\beta Z_1\theta_1\sinh(\theta_2 h_1),$$

$$Z_5=Z_2\sinh(\theta_2 h_1)+\beta Z_2\theta_2\cosh(\theta_2 h_1),\ Z_6=Z_2\cosh(\theta_2 h_1)+\beta Z_2\theta_2\sinh(\theta_2 h_1),$$

$$Z_7=Z_1\sinh(\theta_1 h_2)-\beta Z_1\theta_1\cosh(\theta_1 h_2),\ Z_8=Z_1\cosh(\theta_1 h_2)-\beta Z_1\theta_1\sinh(\theta_1 h_2),$$

$$Z_9=Z_2\sinh(\theta_2 h_2)-\beta Z_2\theta_2\cosh(\theta_2 h_2),\ Z_{10}=Z_2\cosh(\theta_2 h_2)-\beta Z_2\theta_2\sinh(\theta_2 h_2),$$

$$Z_{11}=\cosh(\theta_1 h_1)-\cosh(\theta_1 h_2),\ Z_{12}=\sinh(\theta_1 h_1)-\sinh(\theta_1 h_2),$$

$$Z_{13}=\cosh(\theta_2 h_1)-\cosh(\theta_2 h_2),\ Z_{14}=\sinh(\theta_2 h_1)-\sinh(\theta_2 h_2),$$

$$Z_{15}=\frac{Z_3-\frac{Z_1Z_{11}}{\theta_1(h_1-h2)}}{Z_0},\ Z_{16}=\frac{Z_4-\frac{Z_1Z_{12}}{\theta_1(h_1-h2)}}{Z_0},\ Z_{17}=\frac{Z_5-\frac{Z_2Z_{13}}{\theta_2(h_1-h2)}}{Z_0},\ Z_{18}=\frac{Z_6-\frac{Z_2Z_{14}}{\theta_2(h_1-h2)}}{Z_0}$$

$$Z_{19} = \frac{F}{(h_1 - h2)},\ Z_{20} = \frac{Z_7 - \frac{Z_1 Z_{11}}{\theta_1(h_1 - h2)}}{Z_0},\ Z_{21} = \frac{Z_8 - \frac{Z_1 Z_{12}}{\theta_1(h_1 - h2)}}{Z_0},\ Z_{22} = \frac{Z_9 - \frac{Z_2 Z_{13}}{\theta_2(h_1 - h2)}}{Z_0},$$

$$Z_{23} = \frac{Z_{10} - \frac{Z_2 Z_{14}}{\theta_2(h_1 - h2)}}{Z_0},\ Z_{24} = \cosh(\theta_1 h_1) + Z_{19}\cosh(\theta_1 h_1),\ Z_{25} = Z_{15}\sinh(\theta_1 h_1) - Z_{16}\cosh(\theta_1 h_1)$$

$$Z_{26} = Z_{15}\cosh(\theta_2 h_1) - Z_{17}\cosh(\theta_1 h_1),\ Z_{27} = Z_{15}\sinh(\theta_2 h_1) - Z_{18}\cosh(\theta_1 h_1),$$

$$Z_{28} = \cosh(\theta_1 h_2) + Z_{19}\cosh(\theta_1 h_2),\ Z_{29} = Z_{15}\sinh(\theta_1 h_2) - Z_{16}\cosh(\theta_1 h_2),$$

$$Z_{30} = Z_{15}\cosh(\theta_2 h_2) - Z_{17}\cosh(\theta_1 h_2),\ Z_{31} = Z_{15}\sinh(\theta_2 h_2) - Z_{18}\cosh(\theta_1 h_2),$$

$$Z_{32} = (Z_{15} - Z_{20}) - Z_{19}(Z_{20} - Z_{15}),\ Z_{33} = (Z_{20}Z_{16} - Z_{15}Z_{21}),\ Z_{34} = (Z_{20}Z_{17} - Z_{15}Z_{22}),$$

$$Z_{35} = (Z_{20}Z_{18} - Z_{15}Z_{23}),\ Z_{36} = (Z_{29}Z_{24} - Z_{25}Z_{28}),\ Z_{37} = (Z_{29}Z_{26} - Z_{25}Z_{30}),$$

$$Z_{38} = (Z_{29}Z_{27} - Z_{25}Z_{31}),\ Z_{39} = (Z_{33}Z_{24} - Z_{25}Z_{32}),\ Z_{40} = (Z_{33}Z_{26} - Z_{25}Z_{34}),$$

$$Z_{41} = (Z_{33}Z_{27} - Z_{25}Z_{35}).$$

References

[1] Latham TW (1966). Fluid motion in a peristaltic pumps. M. S. Thesis, MIT, Cambridge. M. A.

[2] Fung YC, and Yih CS (1968). Peristaltic transport. Trans ASME Journal of Applied Mechanics. 35, pp. 669-675.

[3] Burns YC, and Perkes T (1967). Peristaltic Motion. Journal of Fluid Mechanics. 29, pp. 731-743.

[4] Chow TS (1970). Peristaltic transport in a circular cylindrical pipe. Trans ASME Journal of Applied Mechanics. 37, pp. 901-905.

[5] Hung TK, and Brown TD (1976). Solid-Particle Motion in two dimensional peristaltic flows. Journal of Fluid Mechanics. 73, pp. 77-96.

[6] Takabatake S, and Ayukava K (1982). Numerical study of two dimensional peristaltic flows. Journal of Fluid Mechanics. 122, pp. 439-465.

[7] Srivastava LM, and Srivastava VP (1989). Peristaltic transport of a particle-fluid suspension, Trans ASME Journal of Biomechanical Engineering. 111, pp. 157-165.

[8] Misra JC, and Pandey SK (1994). Peristaltic transport of a particle-fluid suspension in a cylindrical tube. Computers & Mathematics with Applications. 28, pp. 131-145.

[9] Misra JC, and Pandey SK (2002). Peristaltic transport of blood in small vessels, Study of mathematical model. Computers & Mathematics with Applications. 43, pp. 1183-1193.

[10] Shapiro AH, Jaffrin MY, and Weinberg SL (1969). Peristaltic pumping with long wave lengths at low Reynolds number. Journal of Fluid Mechanics. 37, pp. 799-825.

[11] Shapiro AH (1987). Pumping and retrograde diffusion in peristaltic walls. Proc. workshop Ureteral Reflux Children, Nat. Acad. Sci., Washington, D. C.

[12] Srivastava LM , and Srivastava VP (1995). Effects of poiseuille flow on peristaltic transport of a particulate suspension. Journal of Applied Mathematics and Physics (ZAMP). 46, pp. 655-679.

[13] Li A, Nesterov NI, Malikova SN, and Kiiatkin VA (1994). The use of an impulsive magnetic field in the combined therapy of patients with stone fragnents in the upper urinary tract. Vopr. Kurortol Fizioter

Lech Fiz Kult. 3, pp. 22-24.

[14] Hakeem A Ei, Naby A Ei, Misiery AEM Ei., and Shamy II Ei (2003). Hydromagnetic flow of fluid with variable viscosity in a uniform tube with peristalsis. Journal of physics A: Mathemetical and General. 36, pp. 8535-8547.

[15] Misra JC, Maiti S, and Shit GC (2008). Peristaltic transport of a physiological fluid in an asymmetric porous channel in the presence of an external magfnetic field. Journal of Mechanics in Medicine and Biology. 8, pp. 507-525.

[16] Wang Y, Ali N, Hayat T, and Oberlack M (2011). Peristaltic motion of a magnetohydrodynamic micropolar fluid in a tube. Applied Mathematical Modelling. 35, pp. 3737-3750.

[17] Shit GC, Roy M, and Ng EYK (2010). Effect of induced magnetic field on peristaltic flow of a micropolar fluid in an asymmetric channel. International Journal for Numerical Methods in Biomedical Engineering. 26, pp. 1380-1403.

[18] Mekheimer KhS (2008a). Effect of the induced magnetic field on peristaltic flow of a couple stress fluid. Physics Letters A. 372, pp. 4271-4278.

[19] Mekheimer KhS (2008b). Peristaltic flow of a magneto-micropolar fluid: Effect of induced magnetic field. Journal of Applied Mathematics. 570825, pp. 23.

[20] Beavers GS, and Joseph DD (1967). Boundary Condition at a Naturally Permeable Wall. Journal of Fluid Mechanics. 30, pp. 197-207.

[21] Tretheway DC, and Meinhart CD (2002). Apparent Fluid Slip at Hydrophobic Microchannels Walls. Physics of Fluids. 14, pp. L9-L12.

[22] Ali N, Hussian Q, Hayat J, and Asghar S(2008). Slip effects on the peristaltic transport of MHD fluid with variable viscosity. Physics Letters A. 372, pp. 1477-1489.

[23] Ali N, Wang Y, Hayat T, and Oberlack M (2009). Slip effects on the peristaltic flow of a third grade fluid in a circular cylindrical tube. ASME Journal of Applied Mechanics. 76, pp. 011006-1-10.

[24] Kumari AVR, and Radhakrishnamacharya G (2012). Effect of slip magnetic field on peristaltic flow in an inclined channel with wall effects. International Journal of Biomathematics. 5, pp. 1250015-1-17. .

[25] Saleem N, Hayat T, and Alsaedil A (2012). Effects of induceed magnetic field and slip condition on peristaltic transport with heat and mass transfer in a non-uniform channel. International Journal of Physical sciences. 7, pp. 191-204.